Nanoscale

PAPER

View Article Online
View Journal | View Issue

Cite this: *Nanoscale*, 2020, **12**, 23191

Synthesis of lead-free $Cs_4(Cd_{1-x}Mn_x)Bi_2Cl_{12}$ ($0 \leq x \leq 1$) layered double perovskite nanocrystals with controlled Mn–Mn coupling interaction†

Hanjun Yang, Wenwu Shi, Tong Cai, Katie Hills-Kimball, Zhenyang Liu, Lacie Dube and Ou Chen *

Received 20th September 2020,
Accepted 22nd October 2020

DOI: 10.1039/d0nr06771g

rsc.li/nanoscale

Lead-free perovskites and their analogues have been extensively studied as a class of next-generation luminescent and optoelectronic materials. Herein, we report the synthesis of new colloidal $Cs_4M(II)Bi_2Cl_{12}$ (M(II) = Cd, Mn) nanocrystals (NCs) with unique luminescence properties. The obtained $Cs_4M(II)Bi_2Cl_{12}$ NCs show a layered double perovskite (LDP) crystal structure with good particle stability. Density functional theory calculations show that both samples exhibit a wide, direct bandgap feature. Remarkably, the strong Mn–Mn coupling effect of the $Cs_4M(II)Bi_2Cl_{12}$ NCs results in an ultra-short Mn photoluminescence (PL) decay lifetime of around 10 μs, around two orders of magnitude faster than commonly observed Mn^{2+} dopant emission in NCs. Diluting the Mn^{2+} ion concentration through forming $Cs_4(Cd_{1-x}Mn_x)Bi_2Cl_{12}$ ($0 < x < 1$) alloyed LDP NCs leads to prolonged PL lifetimes and enhanced PL quantum yields. Our study provides the first synthetic example of Bi-based LDP colloidal NCs with potential for serving as a new category of stable lead-free perovskite-type materials for various applications.

Introduction

Owing to their advantageous optical and optoelectronic properties, lead-halide perovskites (ABX_3, A = methylammonium or MA, Cs, Rb, *etc.*, B = Pb, and X = Cl, Br, I) have been intensively investigated and have triggered a range of applications in the past decade.[1–13] However, the inclusion of the toxic lead element and the intrinsic instability of lead-halide perovskites have set obstacles for the implementation of such materials in a wide range of applications.[14–16] To overcome these drawbacks, searching for possible lead-free perovskites has emerged as an important research subject and has drawn increasing amount of attention in recent years.[17–21] To date, various lead-free perovskites and perovskite analogues have been demonstrated including three-dimensional (3D) double perovskites,[22–25] 2D Ruddlesden–Popper phases,[26,27] Dion–Jacobson phases,[28] and other types of 2D perovskites,[29,30] 0D perovskites,[31–33] vacancy-ordered perovskites,[34,35] and other structures.[36,37] In particular, lead-free perovskite analogues (LFPAs) refer to lead-free materials that possess the characteristic structural motifs of perovskites, *i.e.*, perfect or distorted metal–halide octahedral units, yet do not strictly corner share these units in a cubic framework.[38] Consequently, LFPAs often exhibit crystal structures with reduced symmetries and low dimensionalities which are determined by the manner of geometric connectivity of their metal halide octahedral constituents.[39–41] In addition, given the enlarged compositional space, as well as the structural diversity and versatility of LFPAs, tuning the composition and/or crystal phase of the LFPAs through either direct synthesis or transformation post synthesis has been demonstrated successfully in multiple systems.[32,42,43] Such controllable tuning in materials' composition and thus crystal structure has been validated as a unique and efficient means to manipulate the properties, especially the optoelectronic properties of the LFPA materials, making them an ideal platform for acquiring in-depth understandings of the composition–structure–property relationship of perovskite-type materials.

Very recently, a new class of LFPAs, *i.e.*, vacancy-ordered layered double perovskites (LDPs), has been theoretically predicted and experimentally obtained.[35,44–54] LDPs with a chemical formula of $A_4M(II)M(III)_2X_{12}$ possess a unique crystal structure with a layer of a divalent metal (*e.g.*, M(II) = Cu, Mn, Cd) halide octahedra (*i.e.*, $[M(II)X_6]^{4-}$), sandwiched between two layers of a trivalent metal (*e.g.*, M(III) = Sb, Bi) halide octahedra (*i.e.*, $[M(III)X_6]^{3-}$) (Fig. 1a).[52] The overall tri-layer motifs are separated by top and bottom vacancy layers along the [001] crystal direction of the LDP (Fig. 1a).[44] LDPs possess many unique properties compared to other LFPAs, such as direct band gaps,

Department of Chemistry, Brown University, 324 Brook Street, Providence, Rhode Island 02912, USA. E-mail: ouchen@brown.edu

†Electronic supplementary information (ESI) available. See DOI: 10.1039/d0nr06771g

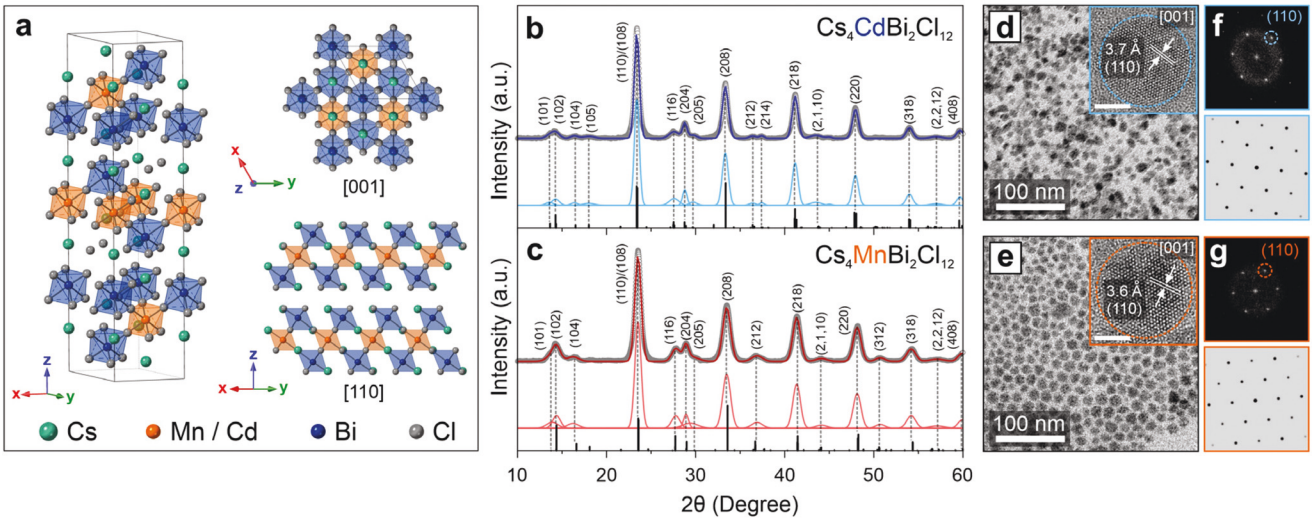

Fig. 1 (a) Schematic illustration of the crystal structure of $Cs_4M(II)Bi_2Cl_{12}$, M(II) = Cd or Mn. Left: A unit cell of trigonal LDP; right: the crystal lattices viewed from the [001] (top) and [110] (bottom) zone axes. (b and c) XRD patterns (grey circles) of the $Cs_4CdBi_2Cl_{12}$ (b) and $Cs_4MnBi_2Cl_{12}$ (c) NCs, fitted curves (blue and red lines) and constituent peaks (cyan and orange lines). Black bars represent the calculated diffraction peak positions. (d and e) TEM images of $Cs_4CdBi_2Cl_{12}$ (d) and $Cs_4MnBi_2Cl_{12}$ (e) NCs. Inset: High-resolution (HR) TEM images, scale bar = 5 nm. (f and g) Fast Fourier transform (FFT) patterns of the corresponding HR TEM images (top) and the simulated electron diffraction patterns viewed from the [001] zone axis (bottom).

improved material stability, rapid and steady photoelectrochemical response, inter- or intra-layer magnetic ordering, p-type conductivity, *etc.*[44,45,48,52] To date, several LDPs have been synthesized in powder or single crystal forms, including $Cs_4M(II)Sb_2Cl_{12}$ (M(II) = Cu, Mn, Cd), $Rb_4M(II)Sb_2Cl_{12}$ (M(II) = Cu, Mn), and $Cs_4M(II)Bi_2Cl_{12}$, (M(II) = Mn, Cd).[32,35,44,47–49,55–57] Examples of bringing such materials down to the nanoscale have been extremely rare. So far, only two examples have been demonstrated, both of which are in Cu/Sb-based systems.[47,48] Kuang *et al.* demonstrated the fabrication of $Cs_4CuSb_2Cl_{12}$ nanocrystals (NCs) using a top-down ultrasonic exfoliation technique, resulting in LDP NCs with reduced effective masses of the photogenerated carriers.[47] Very recently, we reported the first demonstration of the colloidal synthesis of $Cs_4CuSb_2Cl_{12}$ NCs with a direct bandgap of 1.79 eV. Furthermore, an intriguing crystal phase transformation may induce an intriguing indirect-to-direct bandgap transition of these LDPs, which has been explored through adjusting the stoichiometry ratio of Cu and Ag components in $Cs_4Cu_xAg_{(2-2x)}Sb_2Cl_{12}$ NCs.[48]

Herein, we report the first colloidal synthesis of Bi-based LDP NCs using a hot-injection method. Two types of LDP NCs, *i.e.*, $Cs_4MnBi_2Cl_{12}$ and $Cs_4CdBi_2Cl_{12}$ NCs have been successfully synthesized. Density functional theory (DFT) calculations revealed that both samples possess a direct bandgap with a large bandgap energy, consistent with the experimental results. Moreover, we found that the close vicinity of Mn^{2+} ion centers in the $Cs_4MnBi_2Cl_{12}$ NCs induced a strong Mn–Mn coupling, which led to an ultra-short photoluminescence (PL) lifetime and a low PL quantum yield (QY). To control the extent of this strong inter-Mn coupling, we have synthesized a series of $Cs_4(Cd_{1-x}Mn_x)Bi_2Cl_{12}$ cationic alloyed LDP NCs, aiming to dilute the Mn^{2+} ion concentration. The resulting alloyed LDP NCs showed a reduction of the Mn–Mn coupling interaction evidenced by prolonged PL lifetimes and drastically enhanced PL QYs. Our results provide insights into the structure–property relationship of the Cd- and Mn-containing Bi-based LDP NCs, which hold potential for future implementation as a new category of optical and optoelectronic materials in a range of applications.

Results and discussion

Synthesis of $Cs_4M(II)Bi_2Cl_{12}$ (M(II) = Cd, Mn) LDP NCs

Lead-free $Cs_4M(II)Bi_2Cl_{12}$ (M(II) = Cd, Mn) LDP NCs were synthesized using a hot-injection method (see details in the ESI†).[58] Briefly, cesium carbonate, bismuth acetate, and cadmium acetate (or manganese acetate) were mixed in 1-octadecene. Oleic acid and oleylamine with a volume ratio of 3 : 1 were added to the mixture as capping ligands. The mixture was then degassed under vacuum to remove water and oxygen. At 170 °C, benzoyl chloride was injected into the mixture to trigger the nucleation and growth of the NCs. The resultant LDP NCs can be isolated from 1-octadecene by adding isopropanol and further dispersed in non-polar solvents such as toluene.

The trigonal LDP crystal structure with a general formula of $A_4M(II)Bi_2X_{12}$ is derived from the conventional cubic ABX_3 perovskite structure. In short, by replacing the B cations in each (111) crystal plane of the cubic perovskite with a metal ion (either M^{2+} or Bi^{3+}) or a vacancy (V), while keeping the A and X sublattices intact, an alternating Bi–M–Bi–V pattern along the

[001] direction (the original [111] direction of the cubic lattice) of the LDP crystal structure (a trigonal phase) can be formed (Fig. 1a). X-ray diffraction (XRD) patterns of the two samples (*i.e.*, $Cs_4CdBi_2Cl_{12}$ and $Cs_4MnBi_2Cl_{12}$ NCs) unambiguously show trigonal LDP crystal structures (space group: $R\bar{3}m$) with all the Bragg diffraction peaks matching well with the simulated standard peaks (Fig. 1b and c). A set of characteristic triple peaks in the 2θ region of 27°–30° can be assigned to the (116), (204) and (205) crystal planes of the LDP structure (Fig. 1b and c). The lattice parameters of $a = b = 7.574$ Å, $c = 37.36$ Å, and $a = b = 7.542$ Å, $c = 37.16$ Å, were obtained through fitting the XRD patterns for the $Cs_4CdBi_2Cl_{12}$ and $Cs_4MnBi_2Cl_{12}$ LDP NCs, respectively (Fig. S1, S2 and Tables S1, S2†). The slightly larger lattice constant of $Cs_4CdBi_2Cl_{12}$ compared with that of $Cs_4MnBi_2Cl_{12}$ is ascribed to the larger ionic radius of Cd^{2+} (95 pm) than that of Mn^{2+} (83 pm).[59] The broadening effect of all the Bragg diffraction peaks indicated finite crystal domain sizes at the nanometer scale (Tables S1 and S2†). Consistently, the transmission electron microscopy (TEM) images of the $Cs_4M(II)Bi_2Cl_{12}$ NCs show a sphere-like shape with average diameters of 11.8 ± 2.5 nm (in the Cd-containing case) and 11.6 ± 2.1 nm (in the Mn-containing case) (Fig. 1d and e). The displayed *d*-spacings of 3.7 Å and 3.6 Å in the hexagonal lattice fringes for the $Cs_4CdBi_2Cl_{12}$ and $Cs_4MnBi_2Cl_{12}$ NCs, respectively, were assigned to the (110) plane lattice viewed from the [001] zone axis of the trigonal LDP structure (Fig. 1a and d–g). X-ray photoelectron spectroscopy (XPS) measurements confirmed the existence of Cs, Cd/Mn, Bi and Cl in the $Cs_4M(II)Bi_2Cl_{12}$ NCs (Fig. S3†). In addition, the inductively coupled plasma atomic emission spectroscopy (ICP-AES) measurements validated the stoichiometric Bi to M(II) ratio of ~2 (Table S3†). Taken together, these results unequivocally proved the successful synthesis of $Cs_4CdBi_2Cl_{12}$ and $Cs_4MnBi_2Cl_{12}$ LDP NCs. Attempts to incorporate divalent metal ions other than Cd and Mn failed and often resulted in the formation of 2D $Cs_3Bi_2Cl_9$ perovskite-analogue NCs, in line with the theoretical prediction and experimental results of thermodynamically stable bulk Bi-based LDPs.[49,52]

Next, optical property characterization was carried out for both samples. The UV-vis absorption spectra show similar absorption profiles for both samples (Fig. 2a and b). A clear absorption band with a peak at 331 nm (3.75 eV) was observed for the $Cs_4CdBi_2Cl_{12}$ NC sample, while a slightly blue-shifted peak position of 325 nm (3.82 eV) was observed for the $Cs_4MnBi_2Cl_{12}$ NCs (Fig. 2a and b). The corresponding bandgaps were determined by Tauc plot analysis to be 3.49 eV for the $Cs_4CdBi_2Cl_{12}$ NCs and 3.56 eV for the $Cs_4MnBi_2Cl_{12}$ NCs (Fig. 2c and d). The slightly wider bandgap for the $Cs_4MnBi_2Cl_{12}$ NCs can be ascribed to a slightly compressed crystal lattice evidenced by the XRD and HR-TEM results (Fig. 1b–e). These absorption profiles showed a high similarity to those of previously reported 0D Cs_3BiCl_6 NCs with isolated $[BiCl_6]^{3-}$ octahedral units inside the lattice, indicating that the spin forbidden $^1S_0$–$^3P_1$ electronic transition of the Bi^{3+} ion is mainly responsible for the observed absorption band.[40,60]

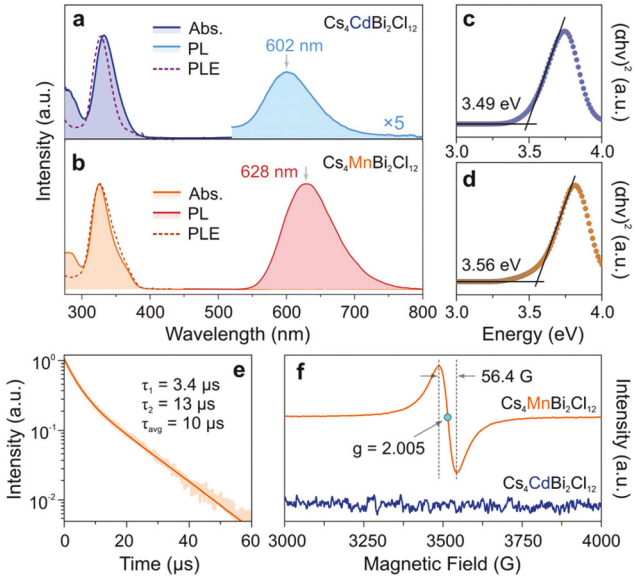

Fig. 2 (a and b) Absorption (Abs.), PL and PLE spectra of $Cs_4CdBi_2Cl_{12}$ (a) and $Cs_4MnBi_2Cl_{12}$ (b) LDP NCs. (c and d) Tauc plots of $Cs_4CdBi_2Cl_{12}$ (c) and $Cs_4MnBi_2Cl_{12}$ (d) NCs. (e) TR-PL decay curve of the $Cs_4MnBi_2Cl_{12}$ NCs. The bi-exponential fitted curve is shown as the orange line. (f) EPR spectra of $Cs_4CdBi_2Cl_{12}$ (bottom) and $Cs_4MnBi_2Cl_{12}$ (top) LDP NCs. The g Factor is determined using the peak center marked with the blue dot.

We further characterized the emission properties of both $Cs_4M(II)Bi_2Cl_{12}$ LDP NCs. A very weak PL emission (centered at ~602 nm, PL QY < 0.1%) was detected for the $Cs_4CdBi_2Cl_{12}$ NCs (Fig. 2a), which can be attributed to the $^3E_g \rightarrow {}^1A_{1g}$ electronic transition of the Cd^{2+} ion in a six-coordinated $[CdCl_6]^{4-}$ octahedral unit, in line with our previous report of Cd-doped $CsPbCl_3$ perovskite NCs.[55] In contrast, a relatively stronger PL emission centered at 628 nm with a PL QY of 0.4% was detected for the $Cs_4MnBi_2Cl_{12}$ LDP NCs (Fig. 2b). This broad orange emission can be assigned to the $^4T_{1g} \rightarrow {}^6A_{1g}$ electronic transition of Mn^{2+} ions in the perovskite NCs.[61,62] The PL excitation (PLE) spectra of both NCs showed nearly overlapped profiles with the corresponding absorption spectra (Fig. 2a and b), confirming an energy transfer process from the photogenerated exciton at the band edge (*i.e.*, conduction band, CB) of the NCs to the Cd^{2+} or Mn^{2+} ions in the $Cs_4M(II)Bi_2Cl_{12}$ LDP NCs. It is worth noting that the PL peak position for the $Cs_4MnBi_2Cl_{12}$ NCs is noticeably redder than that of the Mn-dopant emission from Mn-doped $CsPbCl_3$ perovskite NCs, whose peak is typically in the range of 585–600 nm.[61,63,64] Such a red shift of the Mn emission can be attributed to an inter-Mn-distance-induced Mn–Mn coupling interaction, leading to a larger d–d splitting of the Mn^{2+} ion centers and correspondingly decreasing the gap of the $^4T_{1g} \rightarrow {}^6A_{1g}$ transition. Similar Mn-dopant emission red shifts were observed in the Mn-doped NC samples with a high Mn concentration and/or inhomogeneous Mn distribution.[64–66] This strong Mn–Mn coupling interaction was consistent with the observed low PL QY (*i.e.*, 0.4%) and was further proved by the time-resolved PL (TR-PL) and electron paramagnetic resonance (EPR)

measurements (Fig. 2e and f). While no valid PL decay curves can be collected from the Cd-containing sample due to the low PL intensity (PL QY < 0.1%), a remarkably short PL decay lifetime of ~10 μs was obtained for the $Cs_4MnBi_2Cl_{12}$ NCs (Fig. 2e). Notably, the measured PL lifetime is about two orders of magnitude faster than that of the typical Mn-dopant emission (~1 ms) (Table S4†),[65,67] representing one of the fastest Mn-dopant emission dynamics which have been reported so far.[57,68] While the EPR silence of the $Cs_4CdBi_2Cl_{12}$ NCs is consistent with the absence of unpaired electrons in the sample,[55] a single resonance peak (peak width: 56.4 G; g value: 2.005) was observed for the $Cs_4MnBi_2Cl_{12}$ LDP NCs (Fig. 2f). The single EPR peak signal with the absence of hyperfine splitting was attributed to the strong electron exchange interaction in the sample due to high Mn^{2+} ion concentration, consistent with the optical measurement results discussed above.[67,69,70] The $Cs_4M(II)Bi_2Cl_{12}$ NCs showed a relatively high shelf stability when stored under ambient conditions. The absorption spectra of both $Cs_4CdBi_2Cl_{12}$ and $Cs_4MnBi_2Cl_{12}$ LDP NCs, and the PL spectra of the $Cs_4MnBi_2Cl_{12}$ NCs showed nearly no change up to 30 days (Fig. S4a–c†). The PL intensity of the $Cs_4MnBi_2Cl_{12}$ LDP NCs showed some fluctuation with a slightly increasing trend (Fig. S4d†), possibly caused by NC surface atom rearrangements during storage.

DFT calculations

To gain deeper understandings of the electronic structures of the $Cs_4M(II)Bi_2Cl_{12}$ LDP NCs, their band structures were calculated as shown in Fig. 3 (see the ESI† for calculation details).[71] In the case of $Cs_4CdBi_2Cl_{12}$, no difference in the total energy or electronic structure was found in different magnetic models due to the absence of unpaired electrons. In contrast, in the case of $Cs_4MnBi_2Cl_{12}$, reported experimental results and theoretical calculations show that similar LDP systems commonly possess an intra-layer antiferromagnetic (intra-AFM) ordering due to the presence of 5 unpaired electrons of the Mn^{2+} ion (Mn^{2+}: $[Ar]3d^5$), *i.e.*, antiparallel spin alignment within each $[MnCl_6]^{4-}$ octahedral layer and parallel spin alignment between adjacent layers (Fig. S5†).[49,51,54] Our calculation showed that the intra-AFM model showed the lowest energy among all magnetic ordering models (Table S5†), validating the correctness of employing an intra-AFM model for the band structure calculations. The calculation results (Fig. 3a and b) suggested that, both $Cs_4CdBi_2Cl_{12}$ and $Cs_4MnBi_2Cl_{12}$ showed direct bandgaps located at the Y_2 symmetry point with bandgap energies of 3.55 eV (for the Cd-containing one) and 3.48 eV (for the Mn-containing one), matching well with the experimentally determined values (*i.e.*, 3.49 eV and 3.56 eV,

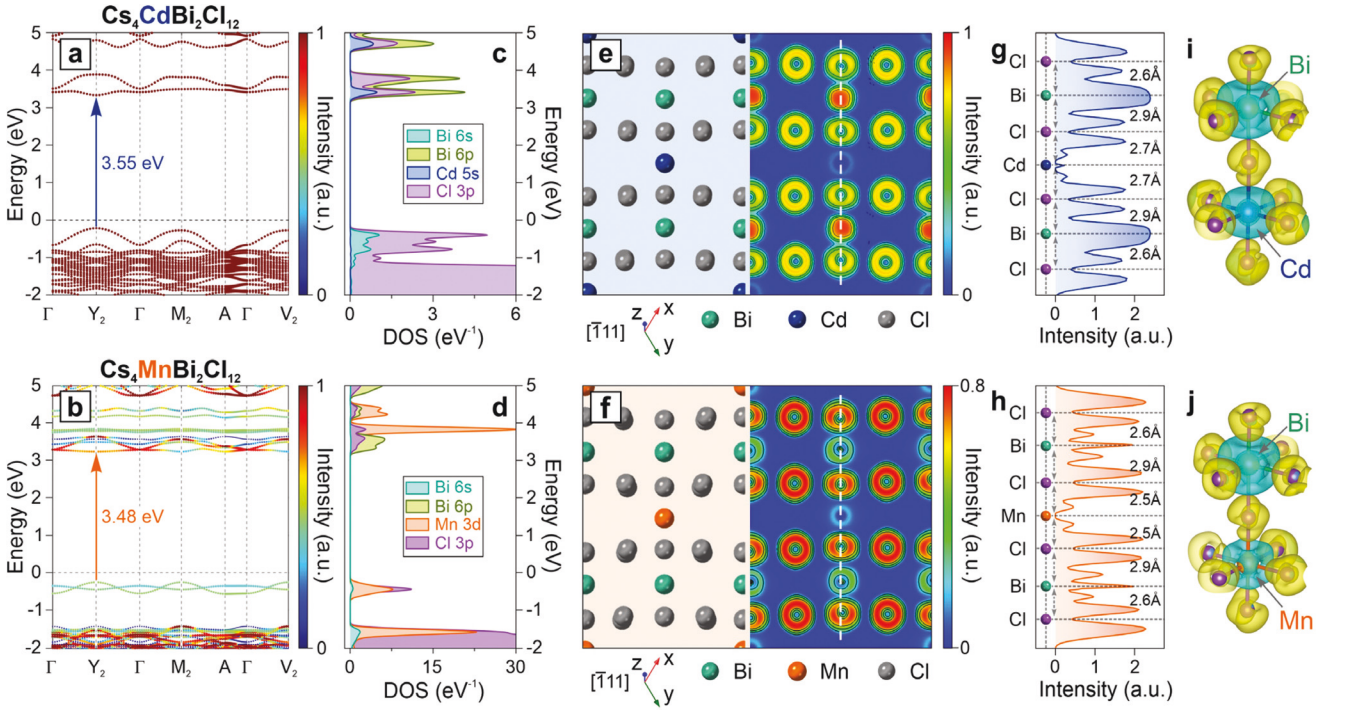

Fig. 3 (a–d) Calculated band structure (a and b) and the corresponding projected density of states (DOS) diagram (c and d) of $Cs_4CdBi_2Cl_{12}$ (a and c) and $Cs_4MnBi_2Cl_{12}$ (b and d) LDPs. Horizontal dashed lines in (a and b) show the Fermi energy level. The colors of the band structure plot represent the Bloch spectral density (spectral weight). (e and f) The electron localization function (ELF) of $Cs_4CdBi_2Cl_{12}$ (e) and $Cs_4MnBi_2Cl_{12}$ (f) LDPs. The atomic crystal structure viewed from the corresponding projections is shown on the left of the ELF diagrams. (g and h) 1D intensity profiles of the ELF along the white dashed lines in (e and f). (i and j) The charge density differences of $Cs_4CdBi_2Cl_{12}$ (i) and $Cs_4MnBi_2Cl_{12}$ (j) LDPs. Yellow and cyan surfaces represent charge gain and charge loss, respectively. Cs atoms are omitted in (e–j) for clear visualization.

Fig. 2c and d). The transitions responsible for the PL emissions in $Cs_4M(II)Bi_2Cl_{12}$ are absent in both calculated band structures, indicating their origin funneled through an energy transfer from the host lattice (*i.e.*, $Cs_4M(II)Bi_2Cl_{12}$ NCs) to the M(II) ion centers,[55,72–77] in accordance with the PLE measurements (Fig. 2a and b). The corresponding density of states (DOS) calculations show that, for the $Cs_4CdBi_2Cl_{12}$ LDP, the conduction band minimum (CBM) mostly consists of Bi 6p, Cl 3p and Cd 5s orbitals, and its valence band maximum (VBM) is composed of Bi 6s and Cl 3p orbitals (Fig. 3c). The CBM of the $Cs_4MnBi_2Cl_{12}$ perovskites is composed of Bi 6p and Cl 3p orbitals, and the VBM contains mostly Mn 3d and Cl 3p orbitals, with a small contribution from the Bi 6s orbital (Fig. 3d). The forbidden transition regulated by both spin and parity spectroscopic selection rules diminishes the Mn 3d orbital contribution (Mn d–d transitions) to electronic transitions,[78] which explains the observed similar absorption spectral profiles (contributed mainly from Bi and Cl orbitals) for both $Cs_4CdBi_2Cl_{12}$ and $Cs_4MnBi_2Cl_{12}$ LDP NCs (Fig. 2a and b).

The electron localization function (ELF) and charge density difference for both $Cs_4CdBi_2Cl_{12}$ and $Cs_4MnBi_2Cl_{12}$ LDPs were calculated and mapped out to gain further insights into the bond characteristics and charge distributions (Fig. 3e–j). The minimal electron density between the metal cations (Bi^{3+}, Cd^{2+}, Mn^{2+}) and Cl^- anions shows the ionic bond nature of the present metal–Cl bonds. In contrast with our recent report on the $Cs_4CuSb_2Cl_{12}$ LDP NCs,[48] no distortions of the $[CdCl_6]^{4-}$ or $[MnCl_6]^{4-}$ octahedral units were observed in both $Cs_4CdBi_2Cl_{12}$ and $Cs_4MnBi_2Cl_{12}$ cases (Fig. 3e and f). However, the $[BiCl_6]^{3-}$ octahedra are distorted, such that the three Bi–Cl bonds (bridging bonds) towards the middle Cd or Mn layers are stretched to a bond length of ~2.90 Å, while the other three bonds (terminal bonds) towards the vacancy layers are compressed to a bond length of ~2.60 Å (Fig. 3g and h). The charge density difference calculations show the electron transfer from Bi^{3+} and Cd^{2+} (or Mn^{2+}) to Cl^-, consistent with the ELF result (Fig. 3i and j). No obvious charge redistribution occurred between the Bi and Cd (or Mn) units (Fig. 3i and j), again confirming the absence of Jahn–Teller distortion in the $Cs_4M(II)Bi_2Cl_{12}$ LDPs unlike in the case of the $Cs_4CuSb_2Cl_{12}$ LDP.[48]

Controlling Mn–Mn coupling in the $Cs_4(Cd_{1-x}Mn_x)Bi_2Cl_{12}$ LDP NCs

The optical and EPR measurements along with the DFT calculation results suggested that the PL behavior of the $Cs_4MnBi_2Cl_{12}$ LDP NCs is largely modulated by the inter-Mn-center distance induced Mn–Mn coupling interaction, signified by the unique layered crystal structure. Therefore, tuning the optical property performance should be feasible through diluting the Mn concentration, thus decoupling the Mn centers inside the LDP NCs. This Mn diluting effect has been recently demonstrated in $Cs_4(Cd_{1-x}Mn_x)Bi_2Cl_{12}$ solid-solution powder samples at the bulk scale by both the Woodward group and the Solis-Ibarra group.[49,57] Significant PL QY enhancements owing to decoupling the Mn–Mn interaction were observed.[57] To examine whether similar effects can be observed at the nanoscale for the LDP particles, a series of $Cs_4(Cd_{1-x}Mn_x)Bi_2Cl_{12}$ alloyed NCs were synthesized *via* mixing the Mn and Cd precursors (*i.e.*, manganese acetate and cadmium acetate) at a controlled stoichiometry ratio during the synthesis (see details in the ESI†). The [Mn]/([Mn] + [Cd]) percentage (%) for the final products was determined to be 0%, 1.7%, 10.1%, 34.9%, 69.0%, and 100% by ICP-AES measurements (Table S3†). In addition, the XPS measurements showed binding energy signals from both Cd 3d and Mn 2p orbitals, further confirming the co-existence of Cd and Mn elements in the $Cs_4(Cd_{1-x}Mn_x)Bi_2Cl_{12}$ NCs (Fig. S6†). TEM and XRD measurements of all the samples showed a similar particle size and shape, as well as the same LDP crystal phase (space group: $R\bar{3}m$) as compared to the Cd- and Mn-pure LDP NCs (Fig. S7† and Fig. 4a). A careful examination of the XRD patterns revealed a continuous shift to lower 2θ angles for all the Bragg diffraction peaks upon decreasing the concentration of the Mn component (Fig. 4b, Fig. S8–S11 and Tables S6–S9†). This result indicated a trend of lattice expansion upon replacing some Mn^{2+} ions with Cd^{2+} ions, in accordance with the relatively larger size of the Cd^{2+} ion compared to that of the Mn^{2+} ion. The calculated lattice parameters increased from a = 7.565 Å to 7.582 Å and from c = 37.09 Å to 37.37 Å (Tables S6–S9†). Correspondingly, the unit cell volume increased from 1838.3 $Å^3$ to 1860.4 $Å^3$ (Fig. 4c). This linear relationship indicates that the unit cell volume evolution as a function of the Mn/Cd ratio is based on Vegard's law,[79–81] suggesting the successful formation of a solid solution of $Cs_4(Cd_{1-x}Mn_x)Bi_2Cl_{12}$ crystals with homogeneously distributed Cd^{2+} and Mn^{2+} ions in individual LDP NCs.

Based on the DFT calculations, the VBM and CBM corresponding to the observed optical transition of $Cs_4(Cd_{1-x}Mn_x)Bi_2Cl_{12}$ are largely determined by the Bi and Cl components. Consistently, altering the stoichiometry ratio between the Cd and Mn components resulted in similar absorption and PLE spectral profiles (Fig. 4e). All the samples showed a similar orange emission with the PL peak maximum centered in the range of 605–628 nm with different emission intensities (Fig. 4d and e). The PL peak blue-shifted continuously upon reducing the Mn concentration from 628 nm for the Mn-only sample to 605 nm for the $Cs_4(Cd_{1-x}Mn_x)Bi_2Cl_{12}$ (x = 1.7%) NCs (Fig. 4d). A slightly redder PL peak compared to that of typical dilute Mn-doped perovskites (~585–600 nm) was likely due to the shorter Mn–Cl bond in the $Cs_4(Cd_{1-x}Mn_x)Bi_2Cl_{12}$ LDP lattice than that in the cubic $CsPbCl_3$ perovskite lattice (2.65 Å *vs.* 2.80 Å), which led to a larger d–d splitting energy with a reduced energy difference between the $^4T_{1g}$ and $^6A_{1g}$ states of Mn^{2+} ions.[64–66] In addition to the PL peak blue-shift, a significant PL QY alteration of the NCs was observed (Fig. 4f). An increase in the PL QY was observed upon diluting Mn with Cd, reaching the highest PL QY of 4.6% for the $Cs_4(Cd_{1-x}Mn_x)Bi_2Cl_{12}$ (x = 34.9%) NCs, an order of magnitude higher compared to the $Cs_4MnBi_2Cl_{12}$ NCs (Fig. 4f). Further diluting the Mn concentration resulted in a decrease in the PL QYs (Fig. 4f). In addition, the PL lifetimes of the $Cs_4(Cd_{1-x}Mn_x)$

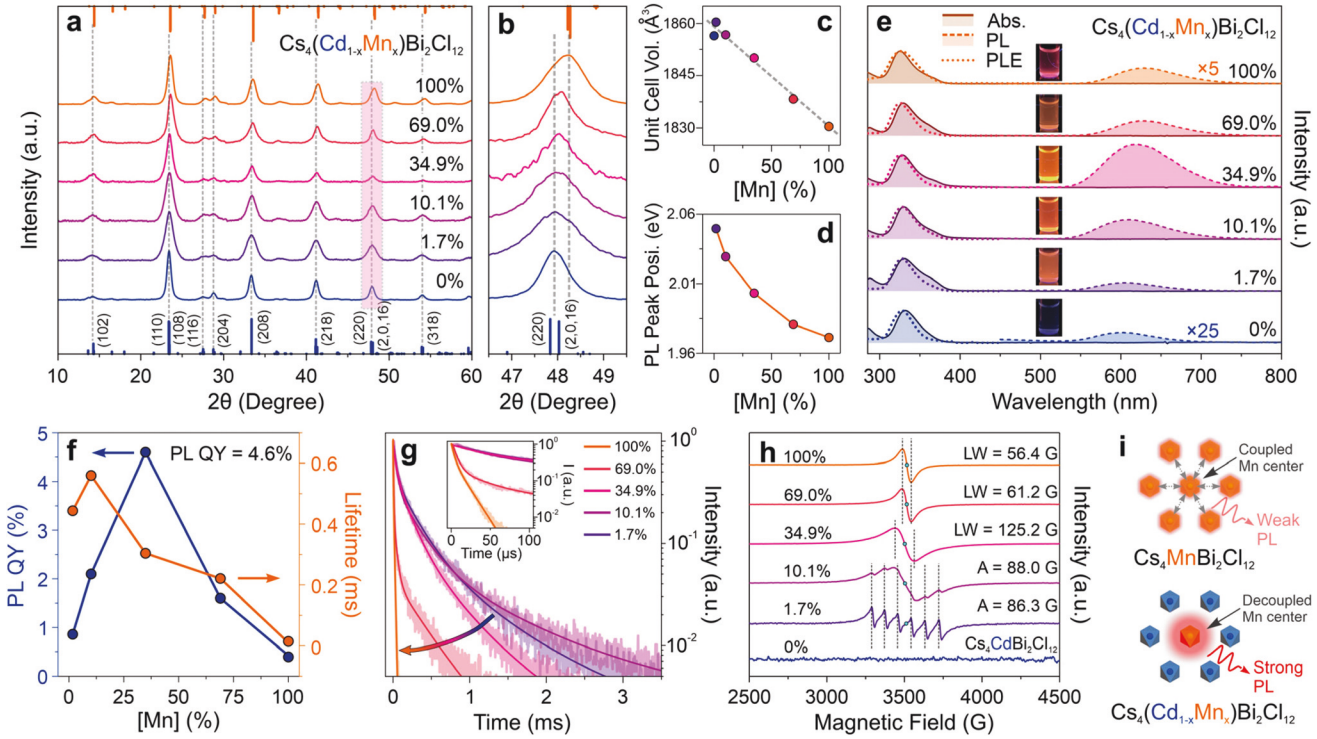

Fig. 4 (a) XRD patterns of $Cs_4(Cd_{1-x}Mn_x)Bi_2Cl_{12}$ (x = 0%, 1.7%, 10.1%, 34.9%, 69.0%, 100%) LDP NCs, and (b) the zoomed-in XRD patterns for the pink rectangular area labeled in (a). (c and d) The evolution of the unit cell volume (unit cell vol., c) and PL peak position (PL peak posi., d) of $Cs_4(Cd_{1-x}Mn_x)Bi_2Cl_{12}$ NCs as a function of Mn concentration ([Mn]%: the percentage of [Mn]/([Cd] + [Mn])). (e) Absorption (Abs.), PL and PLE spectra of $Cs_4(Cd_{1-x}Mn_x)Bi_2Cl_{12}$ LDP NCs. Inset: Photographs of the corresponding NCs dispersed in toluene under UV light. (f) The PL QY (blue) and average PL lifetime (orange) changes as a function of Mn concentration. (g) TR-PL decay curves of the $Cs_4(Cd_{1-x}Mn_x)Bi_2Cl_{12}$ LDP NCs. Inset: The zoomed-in area to show the fast lifetime decay curves. (h) The evolution of the EPR spectra of $Cs_4(Cd_{1-x}Mn_x)Bi_2Cl_{12}$ LDP NCs. (i) Schematic illustration of the Mn–Mn coupling interaction and the PL quenching phenomenon in $Cs_4(Cd_{1-x}Mn_x)Bi_2Cl_{12}$ crystal lattices.

Bi_2Cl_{12} NCs increased from 10 μs to 440 μs with decreasing Mn concentration from x = 100% to x = 1.7% (Fig. 4f and g and Table S4†).[82] This PL lifetime prolongation revealed that the symmetry-orientated spin-exchange interaction, in addition to the Mn–Mn dipole–dipole interaction, was co-responsible for the optical behavior of the $Cs_4MnBi_2Cl_{12}$ NCs.[65,68,72] Together, the PL peak blue-shifting, PL QY variation and PL lifetime prolongation all revealed a Mn^{2+} ion diluting effect with an increasing number of isolated $[MnCl_6]^{4-}$ octahedral units in the crystal lattice. This $[MnCl_6]^{4-}$ octahedral isolation can result in a pseudo-0D structure with decoupled $[MnCl_6]^{4-}$ octahedral units, which impede the energy transfer/loss to adjacent $[MnCl_6]^{4-}$ units, and energy loss through crystalline or surface defect sites of the NCs (Fig. 4i).[68,83,84] Such electronic isolation and magnetic decoupling effects of the $[MnCl_6]^{4-}$ octahedral units were further validated by the EPR measurements,[85] in which a gradual appearance of a six-fold hyperfine splitting EPR pattern was observed for the $Cs_4(Cd_{1-x}Mn_x)Bi_2Cl_{12}$ sample with $x \leq$ 10.1% (Fig. 4h).[67] A measured hyperfine splitting constant of 86.3 G for the $Cs_4(Cd_{1-x}Mn_x)Bi_2Cl_{12}$ (x = 1.7%) sample was consistent with previous reports on octahedrally coordinated Mn species in a perovskite lattice environment.[63,72,86] Furthermore, the experimental results of diluting Mn in the LDP NCs shown above were in good agreement with recent reports,[49,57] as well as our experimental data on the bulk scale Cd/Mn LDP systems (Fig. S12–S15 and Tables S10–S14†). However, the relatively low PL QYs as compared to those of the corresponding bulk counterparts indicated the presence of other fast non-radiative energy relaxation pathways likely induced from the surface sites of the LDP NC samples.[85,87,88]

To further investigate the Mn–Mn coupling effect and optical performance of the $Cs_4(Cd_{1-x}Mn_x)Bi_2Cl_{12}$ LDP NCs, low temperature steady-state and TR-PL measurements were conducted. When the temperature was decreased to 80 K, the PL peak of all the $Cs_4(Cd_{1-x}Mn_x)Bi_2Cl_{12}$ (x = 0%, 1.7%, 10.1%, 34.9%, 69.0%, 100%) NCs red-shifted to longer wavelengths because of the thermal lattice contraction (Fig. 5a and b).[57,89] In general, the NCs with higher Mn concentrations showed larger PL peak red-shifts as compared to the samples with lower Mn concentrations (*e.g.*, ΔE = 64 meV for $Cs_4MnBi_2Cl_{12}$ NCs, and ΔE = 49 meV for $Cs_4(Cd_{0.98}Mn_{0.02})Bi_2Cl_{12}$ NCs). A similar trend has been observed in the bulk $Cs_4(Cd_{1-x}Mn_x)Bi_2Cl_{12}$ powder samples as well.[57] A universal PL peak narrowing effect (24%–29% narrowing in the FWHM) was also observed for all the samples at 80 K (Fig. S16†), and was induced by diminishing the electron–photon coupling (mainly electron–longitudinal optical phonon coupling) upon lowering

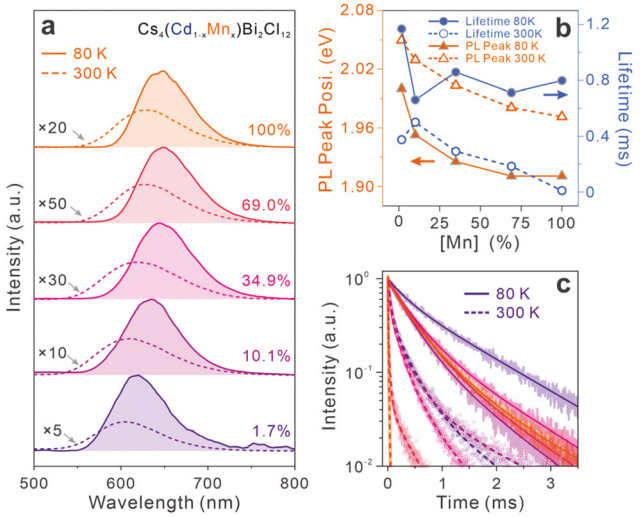

Fig. 5 (a) PL spectra of $Cs_4(Cd_{1-x}Mn_x)Bi_2Cl_{12}$ (x = 0%, 1.7%, 10.1%, 34.9%, 69.0%, and 100%) LDP NCs at low temperature (at 80 K, solid lines) and room temperature (dashed line). (b) The evolution of the PL peak position (PL peak posi., orange) and average PL lifetime (blue) with different Mn concentrations. Solid circles and triangles represent the data obtained at low temperature (*i.e.*, 80 K), and open circles and triangles represent the data obtained at room temperature. (c) TR-PL decay curves of the $Cs_4(Cd_{1-x}Mn_x)Bi_2Cl_{12}$ LDP NCs measured at low temperature (solid lines) and room temperature (dashed lines).

the temperature.[89,90] This suppression of electron–phonon coupling was further confirmed by the significant enhancement of the PL intensities of the samples (~13–98-fold increase, Fig. 5a, and Fig. S17†), which was likely co-induced by the elimination of some non-radiative recombination channels,[57,87] in line with the prolonged PL lifetimes at a low temperature of 80 K (Fig. 5b, c and Table S15†). We also noted that all samples showed similar average PL lifetimes (0.7–1.2 ms) at 80 K, which could be ascribed to a competing effect between the suppression of the fast non-radiative channel (*i.e.*, prolonging PL lifetime) and the Mn–Mn interaction (*i.e.*, shortening PL lifetime).

Conclusions

To conclude, we present the first example of the colloidal syntheses of $Cs_4M(II)Bi_2Cl_{12}$ (M(II) = Cd, Mn) LDP NCs. Both types of NC samples possess a spherical-like shape with a trigonal LDP crystal structure. DFT calculations reveal wide and direct bandgap structures for both LDPs with no octahedral distortions for the $[M(II)Cl_6]^{4-}$ units. Due to the high Mn concentration dictated by the stoichiometry and layered octahedral lattice feature of the crystal structure, the $Cs_4MnBi_2Cl_{12}$ NCs exhibit strong Mn–Mn interaction-dictated optical and magnetic properties. By forming a series of $Cs_4(Cd_{1-x}Mn_x)Bi_2Cl_{12}$ ($0 < x < 1$) cationic alloyed LDP NCs, the Mn–Mn coupling interaction can be effectively reduced, resulting in more isolated $[MnCl_6]^{4-}$ octahedral units inside the crystal lattice. Consistent with the studies on bulk scale materials, such a Mn component diluting effect induced electronic and magnetic decoupling process leads to significantly enhanced PL QYs with the highest value of 4.6% and prolonged PL lifetimes of the LDP NCs. Such a family of colloidal NC materials holds potential to be developed as a new generation of optical and optoelectronic materials with solution processability. The inclusion of the toxic Cd element may hinder their future application implementation. More efforts on searching for non-toxic replacements and developing the corresponding synthetic chemistry are still a pressing need.

Conflicts of interest

There are no conflicts to declare.

Acknowledgements

O. C. acknowledges the support from the Brown University startup fund, the 3M non-tenured faculty award fund and the Camille & Henry Dreyfus Foundation through the Camille Dreyfus Teacher-Scholar Awards program. O. C. also acknowledges the National Science Foundation (DMR-1943930 and CBET-1936223). K. H.-K. is supported by the U.S. Department of Education GAANN research fellowship (P200A150037). L. D. thanks the support from the Brown IMSD fellowship program through NIGMS (R25GM083270). TEM, XRD, EPR and XPS measurements were performed at the Electron Microscopy Facility and NanoTools Facility in the Institute for Molecular and Nanoscale Innovation (IMNI) at Brown University. ICP-AES were measured in the Environmental Chemistry Facilities in Brown University. The computational analyses of this research were conducted using computational resources and services at the Brown University Center for Computation and Visualization (CCV).

References

1 A. Kojima, K. Teshima, Y. Shirai and T. Miyasaka, *J. Am. Chem. Soc.*, 2009, **131**, 6050–6051.
2 Z.-K. Tan, R. S. Moghaddam, M. L. Lai, P. Docampo, R. Higler, F. Deschler, M. Price, A. Sadhanala, L. M. Pazos, D. Credgington, F. Hanusch, T. Bein, H. J. Snaith and R. H. Friend, *Nat. Nanotechnol.*, 2014, **9**, 687–692.
3 J. Song, J. Li, X. Li, L. Xu, Y. Dong and H. Zeng, *Adv. Mater.*, 2015, **27**, 7162–7167.
4 L. Protesescu, S. Yakunin, M. I. Bodnarchuk, F. Krieg, R. Caputo, C. H. Hendon, R. X. Yang, A. Walsh and M. V. Kovalenko, *Nano Lett.*, 2015, **15**, 3692–3696.
5 Q. A. Akkerman, V. D'Innocenzo, S. Accornero, A. Scarpellini, A. Petrozza, M. Prato and L. Manna, *J. Am. Chem. Soc.*, 2015, **137**, 10276–10281.

6 G. Nedelcu, L. Protesescu, S. Yakunin, M. I. Bodnarchuk, M. J. Grotevent and M. V. Kovalenko, *Nano Lett.*, 2015, **15**, 5635–5640.
7 H. C. Cho, S. H. Jeong, M. H. Park, Y. H. Kim, C. Wolf, C. L. Lee, J. H. Heo, A. Sadhanala, N. Myoung, S. Yoo, S. H. Im, R. H. Friend and T. W. Lee, *Science*, 2015, **350**, 1222–1225.
8 A. Swarnkar, R. Chulliyil, V. K. Ravi, M. Irfanullah, A. Chowdhury and A. Nag, *Angew. Chem., Int. Ed.*, 2015, **54**, 15424–15428.
9 K. Hills-Kimball, Y. Nagaoka, C. Cao, E. Chaykovsky and O. Chen, *J. Mater. Chem. C*, 2017, **5**, 5680–5684.
10 F. Zhang, H. Zhong, C. Chen, X.-g. Wu, X. Hu, H. Huang, J. Han, B. Zou and Y. Dong, *ACS Nano*, 2015, **9**, 4533–4542.
11 Y. Nagaoka, K. Hills-Kimball, R. Tan, R. Li, Z. Wang and O. Chen, *Adv. Mater.*, 2017, **29**, 1606666.
12 H. L. Huang, F. C. Zhao, L. G. Liu, F. Zhang, X. G. Wu, L. J. Shi, B. S. Zou, Q. B. Pei and H. Z. Zhong, *ACS Appl. Mater. Interfaces*, 2015, **7**, 28128–28133.
13 Y. Yuan, H. Zhu, K. Hills-Kimball, T. Cai, W. Shi, Z. Wei, H. Yang, Y. Candler, P. Wang, J. He and O. Chen, *Angew. Chem., Int. Ed.*, 2020, **59**, 2–9.
14 A. Babayigit, A. Ethirajan, M. Muller and B. Conings, *Nat. Mater.*, 2016, **15**, 247.
15 Y. Wei, Z. Cheng and J. Lin, *Chem. Soc. Rev.*, 2019, **48**, 310–350.
16 S. Wang, L. Du, Z. Jin, Y. Xin and H. Mattoussi, *J. Am. Chem. Soc.*, 2020, **142**, 12669–12680.
17 J. Sun, J. Yang, J. I. Lee, J. H. Cho and M. S. Kang, *J. Phys. Chem. Lett.*, 2018, **9**, 1573–1583.
18 L. Liang and P. Gao, *Adv. Sci.*, 2018, **5**, 1700331.
19 W. Ke and M. G. Kanatzidis, *Nat. Commun.*, 2019, **10**, 965.
20 Z. Xiao, Z. Song and Y. Yan, *Adv. Mater.*, 2019, **31**, 1803792.
21 Q. Fan, G. V. Biesold-McGee, J. Ma, Q. Xu, S. Pan, J. Peng and Z. Lin, *Angew. Chem.*, 2020, **59**, 1030–1046.
22 E. T. McClure, M. R. Ball, W. Windl and P. M. Woodward, *Chem. Mater.*, 2016, **28**, 1348–1354.
23 G. Volonakis, A. A. Haghighirad, R. L. Milot, W. H. Sio, M. R. Filip, B. Wenger, M. B. Johnston, L. M. Herz, H. J. Snaith and F. Giustino, *J. Phys. Chem. Lett.*, 2017, **8**, 772–778.
24 S. E. Creutz, E. N. Crites, M. C. De Siena and D. R. Gamelin, *Nano Lett.*, 2018, **18**, 1118–1123.
25 Y. Bekenstein, J. C. Dahl, J. Huang, W. T. Osowiecki, J. K. Swabeck, E. M. Chan, P. Yang and A. P. Alivisatos, *Nano Lett.*, 2018, **18**, 3502–3508.
26 J. Qiu, Y. Xia, Y. Zheng, W. Hui, H. Gu, W. Yuan, H. Yu, L. Chao, T. Niu, Y. Yang, X. Gao, Y. Chen and W. Huang, *ACS Energy Lett.*, 2019, **4**, 1513–1520.
27 E. T. McClure, A. P. McCormick and P. M. Woodward, *Inorg. Chem.*, 2020, **59**, 6010–6017.
28 P. Li, X. Liu, Y. Zhang, C. Liang, G. Chen, F. Li, M. Su, G. Xing, X. Tao and Y. Song, *Angew. Chem.*, 2020, **59**, 6909–6914.
29 M. Leng, Z. Chen, Y. Yang, Z. Li, K. Zeng, K. Li, G. Niu, Y. He, Q. Zhou and J. Tang, *Angew. Chem., Int. Ed.*, 2016, **55**, 15012–15016.
30 J. Zhang, Y. Yang, H. Deng, U. Farooq, X. Yang, J. Khan, J. Tang and H. Song, *ACS Nano*, 2017, **11**, 9294–9302.
31 K. M. McCall, C. C. Stoumpos, S. S. Kostina, M. G. Kanatzidis and B. W. Wessels, *Chem. Mater.*, 2017, **29**, 4129–4145.
32 S. E. Creutz, H. Liu, M. E. Kaiser, X. Li and D. R. Gamelin, *Chem. Mater.*, 2019, **31**, 4685–4697.
33 W. Shi, T. Cai, Z. Wang and O. Chen, *J. Chem. Phys.*, 2020, **153**, 141101.
34 M. Chen, M.-G. Ju, A. D. Carl, Y. Zong, R. L. Grimm, J. Gu, X. C. Zeng, Y. Zhou and N. P. Padture, *Joule*, 2018, **2**, 558–570.
35 B. Vargas, E. Ramos, E. Pérez-Gutiérrez, J. C. Alonso and D. Solis-Ibarra, *J. Am. Chem. Soc.*, 2017, **139**, 9116–9119.
36 T. Jun, K. Sim, S. Iimura, M. Sasase, H. Kamioka, J. Kim and H. Hosono, *Adv. Mater.*, 2018, **30**, 1804547.
37 L. Zhou, J.-F. Liao, Z.-G. Huang, J.-H. Wei, X.-D. Wang, W.-G. Li, H.-Y. Chen, D.-B. Kuang and C.-Y. Su, *Angew. Chem., Int. Ed.*, 2019, **58**, 5277–5281.
38 L. Etgar, *Energy Environ. Sci.*, 2018, **11**, 234–242.
39 Z. Xiao, W. Meng, J. Wang, D. B. Mitzi and Y. Yan, *Mater. Horiz.*, 2017, **4**, 206–216.
40 H. Yang, T. Cai, E. Liu, K. Hills-Kimball, J. Gao and O. Chen, *Nano Res.*, 2020, **13**, 282–291.
41 B. Billstrand, K. Bian, C. Karler, D. Ye, A. Hwang and H. Fan, *MRS Adv.*, 2018, **3**, 2825–2831.
42 Y. Lou, M. Fang, J. Chen and Y. Zhao, *Chem. Commun.*, 2018, **54**, 3779–3782.
43 K. M. McCall, C. C. Stoumpos, O. Y. Kontsevoi, G. C. B. Alexander, B. W. Wessels and M. G. Kanatzidis, *Chem. Mater.*, 2019, **31**, 2644–2650.
44 B. Vargas, R. Torres-Cadena, J. Rodríguez-Hernández, M. Gembicky, H. Xie, J. Jiménez-Mier, Y.-S. Liu, E. Menéndez-Proupin, K. R. Dunbar, N. Lopez, P. Olalde-Velasco and D. Solis-Ibarra, *Chem. Mater.*, 2018, **30**, 5315–5321.
45 J. Xu, J.-B. Liu, J. Wang, B.-X. Liu and B. Huang, *Adv. Funct. Mater.*, 2018, **28**, 1800332.
46 N. Singhal, R. Chakraborty, P. Ghosh and A. Nag, *Chem. – Asian J.*, 2018, **13**, 2085–2092.
47 X.-D. Wang, N.-H. Miao, J.-F. Liao, W.-Q. Li, Y. Xie, J. Chen, Z.-M. Sun, H.-Y. Chen and D.-B. Kuang, *Nanoscale*, 2019, **11**, 5180–5187.
48 T. Cai, W. Shi, S. Hwang, K. Kobbekaduwa, Y. Nagaoka, H. Yang, K. Hills-Kimball, H. Zhu, J. Wang, Z. Wang, Y. Liu, D. Su, J. Gao and O. Chen, *J. Am. Chem. Soc.*, 2020, **142**, 11927–11936.
49 N. P. Holzapfel, J. D. Majher, T. A. Strom, C. E. Moore and P. M. Woodward, *Chem. Mater.*, 2020, **32**, 3510–3516.
50 T. T. Tran, C. A. Pocs, Y. Zhang, M. J. Winiarski, J. Sun, M. Lee and T. M. McQueen, *Phys. Rev. B: Condens. Matter Mater. Phys.*, 2020, **101**, 235107.

51 D. Han, T. Zhang and S. Chen, *J. Phys.: Condens. Matter*, 2020, **32**, 225705.
52 B. Vargas, R. Torres-Cadena, D. T. Reyes-Castillo, J. Rodríguez-Hernández, M. Gembicky, E. Menéndez-Proupin and D. Solis-Ibarra, *Chem. Mater.*, 2020, **32**, 424–429.
53 P. M. Jayasankar, A. K. Pathak, S. P. Madhusudanan, S. Murali and S. K. Batabyal, *Mater. Lett.*, 2020, **263**, 127200.
54 X. Wang, W. Meng, Z. Xiao, J. Wang, D. Mitzi and Y. Yan, arXiv, 2017, preprint, arXiv:1707.09539, https://arxiv.org/abs/1707.09539.
55 T. Cai, H. Yang, K. Hills-Kimball, J.-P. Song, H. Zhu, E. Hofman, W. Zheng, B. M. Rubenstein and O. Chen, *J. Phys. Chem. Lett.*, 2018, **9**, 7079–7084.
56 J.-H. Wei, J.-F. Liao, X.-D. Wang, L. Zhou, Y. Jiang and D.-B. Kuang, *Matter*, 2020, **3**, 892–903.
57 B. Vargas, D. T. Reyes-Castillo, E. Coutino-Gonzalez, C. Sánchez-Aké, C. Ramos, C. Falcony and D. Solis-Ibarra, *Chem. Mater.*, 2020, **32**, 9307–9315.
58 M. Imran, V. Caligiuri, M. Wang, L. Goldoni, M. Prato, R. Krahne, L. De Trizio and L. Manna, *J. Am. Chem. Soc.*, 2018, **140**, 2656–2664.
59 R. Shannon, *Acta Crystallogr., Sect. A: Cryst. Phys., Diffr., Theor. Gen. Crystallogr.*, 1976, **32**, 751–767.
60 S. Radhakrishna and R. S. S. Setty, *Phys. Rev. B: Solid State*, 1976, **14**, 969–976.
61 W. Liu, Q. Lin, H. Li, K. Wu, I. Robel, J. M. Pietryga and V. I. Klimov, *J. Am. Chem. Soc.*, 2016, **138**, 14954–14961.
62 B. Luo, Y. Guo, X. Li, Y. Xiao, X. Huang and J. Z. Zhang, *J. Phys. Chem. C*, 2019, **123**, 14239–14245.
63 X. Yuan, S. Ji, M. C. De Siena, L. Fei, Z. Zhao, Y. Wang, H. Li, J. Zhao and D. R. Gamelin, *Chem. Mater.*, 2017, **29**, 8003–8011.
64 H. Liu, Z. Wu, J. Shao, D. Yao, H. Gao, Y. Liu, W. Yu, H. Zhang and B. Yang, *ACS Nano*, 2017, **11**, 2239–2247.
65 J. F. Suyver, S. F. Wuister, J. J. Kelly and A. Meijerink, *Phys. Chem. Chem. Phys.*, 2000, **2**, 5445–5448.
66 J.-C. Zhang, L.-Z. Zhao, Y.-Z. Long, H.-D. Zhang, B. Sun, W.-P. Han, X. Yan and X. Wang, *Chem. Mater.*, 2015, **27**, 7481–7489.
67 A. De, N. Mondal and A. Samanta, *Nanoscale*, 2017, **9**, 16722–16727.
68 Y. Liu, J. Zhang, B. Han, X. Wang, Z. Wang, C. Xue, G. Bian, D. Hu, R. Zhou, D.-S. Li, Z. Wang, Z. Ouyang, M. Li and T. Wu, *J. Am. Chem. Soc.*, 2020, **142**, 6649–6660.
69 P. A. Gonzalez Beermann, B. R. McGarvey, S. Muralidharan and R. C. W. Sung, *Chem. Mater.*, 2004, **16**, 915–918.
70 A. B. Mahmoud, H. J. von Bardeleben, J. L. Cantin, A. Mauger, E. Chikoidze and Y. Dumont, *Phys. Rev. B: Condens. Matter Mater. Phys.*, 2006, **74**, 115203.
71 A. V. Krukau, O. A. Vydrov, A. F. Izmaylov and G. E. Scuseria, *J. Chem. Phys.*, 2006, **125**, 224106.
72 K. Hills-Kimball, M. J. Pérez, Y. Nagaoka, T. Cai, H. Yang, A. H. Davis, W. Zheng and O. Chen, *Chem. Mater.*, 2020, **32**, 2489–2500.
73 N. Chen, T. Cai, W. Li, K. Hills-Kimball, H. Yang, M. Que, Y. Nagaoka, Z. Liu, D. Yang, A. Dong, C.-Y. Xu, R. Zia and O. Chen, *ACS Appl. Mater. Interfaces*, 2019, **11**, 16855–16863.
74 R. Bakthavatsalam, A. Biswas, M. Chakali, P. R. Bangal, B. P. Kore and J. Kundu, *J. Phys. Chem. C*, 2019, **123**, 4739–4748.
75 V. Pinchetti, A. Anand, Q. A. Akkerman, D. Sciacca, M. Lorenzon, F. Meinardi, M. Fanciulli, L. Manna and S. Brovelli, *ACS Energy Lett.*, 2019, **4**, 85–93.
76 A. H. Davis, E. Hofman, K. Chen, Z.-J. Li, A. Khammang, H. Zamani, J. M. Franck, M. M. Maye, R. W. Meulenberg and W. Zheng, *Chem. Mater.*, 2019, **31**, 2516–2523.
77 T. Cai, J. Wang, W. Li, K. Hills-Kimball, H. Yang, Y. Nagaoka, Y. Yuan, R. Zia and O. Chen, *Adv. Sci.*, 2020, **7**, 2001317.
78 K. Xu, C. C. Lin, X. Xie and A. Meijerink, *Chem. Mater.*, 2017, **29**, 4265–4272.
79 Y. Yuan, H. Zhu, X. Wang, D. Cui, Z. Gao, D. Su, J. Zhao and O. Chen, *Chem. Mater.*, 2019, **31**, 2635–2643.
80 A. R. Denton and N. W. Ashcroft, *Phys. Rev. A*, 1991, **43**, 3161–3164.
81 B. Su, M. S. Molokeev and Z. Xia, *J. Phys. Chem. Lett.*, 2020, **11**, 2510–2517.
82 D. Rossi, D. Parobek, Y. Dong and D. H. Son, *J. Phys. Chem. C*, 2017, **121**, 17143–17149.
83 H. Shao, X. Bai, H. Cui, G. Pan, P. Jing, S. Qu, J. Zhu, Y. Zhai, B. Dong and H. Song, *Nanoscale*, 2018, **10**, 1023–1029.
84 L. R. Bradshaw, J. W. May, J. L. Dempsey, X. Li and D. R. Gamelin, *Phys. Rev. B: Condens. Matter Mater. Phys.*, 2014, **89**, 115312.
85 X. Yang, C. Pu, H. Qin, S. Liu, Z. Xu and X. Peng, *J. Am. Chem. Soc.*, 2019, **141**, 2288–2298.
86 T. Qiao, D. Parobek, Y. Dong, E. Ha and D. H. Son, *Nanoscale*, 2019, **11**, 5247–5253.
87 S. Ji, X. Yuan, S. Cao, W. Ji, H. Zhang, Y. Wang, H. Li, J. Zhao and B. Zou, *J. Phys. Chem. Lett.*, 2020, **11**, 2142–2149.
88 Z. Quan, Z. Wang, P. Yang, J. Lin and J. Fang, *Inorg. Chem.*, 2007, **46**, 1354–1360.
89 J. Yi, X. Ge, E. Liu, T. Cai, C. Zhao, S. Wen, H. Sanabria, O. Chen, A. M. Rao and J. Gao, *Nanoscale Adv.*, 2020, **2**, 4390–4394.
90 A. Shinde, R. Gahlaut and S. Mahamuni, *J. Phys. Chem. C*, 2017, **121**, 14872–14878.